Aerodynamic Analysis of the Flying V Subsonic Transport to Enable Engine Integration

Kumar, Ankit; Asaro, S.; Vos, Roelof

DOI
10.2514/6.2025-0666

Publication date
2025

Document Version
Final published version

Published in
Proceedings of the AIAA SCITECH 2025 Forum

AIAA SciTech Forum
6-10 January 2025, Orlando, FL
AIAA SCITECH 2025 Forum

10.2514/6.2025-0666

Aerodynamic Analysis of the Flying V Subsonic Transport to Enable Engine Integration

Ankit Kumar*, Salvatore Asaro† and Roelof Vos‡
Delft University of Technology, Kluyverweg 1 2629HS, Delft, The Netherlands

The Flying V is a flying-wing aircraft that has 20% less cruise drag than a modern tube-and-wing aircraft. The integration of the over-the-wing engine is not trivial due to the strong aerodynamic interaction between the wing and inlet. Prior to integrating the engine, the aerodynamics of the Flying V are studied with a Reynolds-averaged Navier-Stokes (RANS) solver using a finite-volume mesh. Engine dimensions are sized through rubber sizing for the take-off thrust rating. The analysis focuses on the flow characteristics on the upper surface of the wing, particularly in the region where the engine could be located. Forces and pressure changes induced at different angles of attack and flight conditions are studied. Subsequently, the evolution of the boundary layer at different locations is analyzed to understand the flow that the engine would face at the inlet. For the defined inlet dimensions, the inlet distortion is evaluated at various locations on the wing. Preferred regions for engine placement and integration approaches are proposed and discussed to maximize the engine inlet performance at on-design and off-design conditions.

Nomenclature

b	span (m)	Z	length in vertical direction (m)
c	chord (m)	M	Mach number
$\overline{c}$	mean aerodynamic chord (m)	α	angle of attack $(^\circ)$
C_D	drag coefficient	ω	vorticity $(1/s)$
C_L	lift coefficient	δ_{99}	boundary layer thickness (m)
C_M	moment coefficient	∞	infinity
C_p	pressure coefficient	M_∞	free stream Mach number
D	drag (N)	θ	angle $(^\circ)$
L	lift (N)	DC	Distortion Coefficient
h	altitude (m)	FW	Flying Wing
p	pressure (Pa)	TEV	Trailing edge vortex
p_t	total pressure (Pa)	IBV	Inboard vortex
Re	Reynolds number	BWB	Blended Wing-Body
Re_c	chord-based Reynolds number	FVM	Finite Volume Method
$Re_{\overline{c}}$	mean aerodynamic chord Reynolds number	MUSCL	Monotonic Upstream-centered Scheme for Conservation Laws
S	wing reference area (m^2)		
T	thrust (kN)	MTOM	Maximum Take-off Mass
U_∞	freestream velocity (m/s)	NZE	Net Zero Emissions
U	velocity component in the X direction (m/s)	RANS	Reynolds-Averaged Navier-Stokes
V	velocity component in the Y direction (m/s)	Roe-FDS	Roe flux-difference splitting
W	weight (kg)	SAF	Sustainable Aviation Fuels
X	length in streamwise direction(m)	SST	shear stress transport
Y	length in perpendicular to streamwise direction (m)	HEFA	Hydroprocessed Esters and Fatty Acids

*PhD Candidate, Faculty of Aerospace Engineering, AIAA Member
†Postdoctoral Researcher, Faculty of Aerospace Engineering
‡Associate Professor, Faculty of Aerospace Engineering, AIAA Associate Fellow

I. Introduction

Aviation, evolving since its landmark inaugural flight in 1903, has undergone profound advancements across aircraft and engine designs, supported by extensive research. A salient feature in civilian transport aircraft is the tube-and-wing configuration, which has remained consistent for over 70 years. Significant strides in engine efficiency, aerostructures, and avionics have made air transportation faster, safer, and more affordable. Despite these advancements, aviation's contribution to energy-related emissions, approximately 2%, necessitates urgent action. Jet aircraft are responsible for 95% of commercial aviation greenhouse gas emissions, with sustainable aviation fuel (SAF) being the only viable near-term solution for decarbonization. The SAF Grand Challenge aims to produce 3 billion gallons annually by 2030, primarily through lipid-based pathways (HEFA), and 35 billion gallons by 2050 by incorporating waste-based Fischer–Tropsch (FT) and alcohol-to-jet processes[1]. In the Net Zero Emissions (NZE) Scenario, behavioral changes are equally critical, as total aviation activity would otherwise increase by 10% by 2030 and over 20% by 2050. Achieving NZE goals also relies on innovative technologies to achieve a 2% annual reduction in fuel intensity by 2050. These challenges underscore the essential role of continuous innovation and research in steering aviation towards sustainability [2]. Building on this imperative, NASA's N+3 program, initiated in 2008, explores novel airframe designs targeting a 70% reduction in fuel burn compared to contemporary airliners [3]. One such design, the D8 transport jet, incorporates a high-aspect-ratio wing and embedded engine installation, resulting in a 33% decrease in fuel burn. Other configurations, such as Blended Wing-Body (BWB) and flying wing aircraft, achieve higher lift-to-drag ratios and reduced fuel consumption, surpassing traditional tube-and-wing designs. For instance, the Blended Wing-Body (BWB), funded by NASA Langley Research Center, outperforms the A380-700 with a 15% reduction in takeoff weight and a significant 27% reduction in fuel burn per seat mile [4].

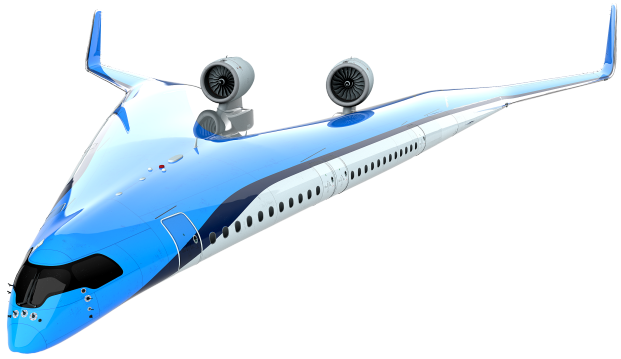

Fig. 1 Artist impression of the Flying V

In line with these advancements, another notable endeavor towards achieving Net Zero Emissions (NZE) by 2050 is underway at TU Delft. The university is leading the development of a transport flying wing aircraft known as the Flying V. This innovative design aims to significantly improve efficiency, boasting a higher lift-to-drag ratio that can reduce fuel burn by 20% compared to conventional aircraft like the A350-1000. Conceived by Benad in 2015 [5] and further developed by TU Delft, the Flying V has an over-the-wing-engine and integrates various components into its wing structure, including the passenger cabin, cargo hold, and fuel volume, thus offering a promising step toward a more sustainable future in aviation.

Research at TU Delft on the Flying V aircraft has primarily centered on enhancing the lift-to-drag ratio [6][7], particularly the cruise conditions. There have been limited investigations aimed at understanding and performing engine integration. One notable study by [8] explored aerodynamic performance during engine integration by analyzing the lift-to-drag (L/D) ratio for various engine placements. Utilizing Euler methods, the research identified an optimal engine location, as illustrated in Figure 2a.

The research highlighted that misplacing the engine could detrimentally impact the Lift-to-Drag (L/D) ratio up to 55% and estimated an aerodynamic penalty of 10% upon integration. In addition, reducing the space between the nacelles of the two engines makes the flow behave as if passing through a convergent-divergent channel, forming strong

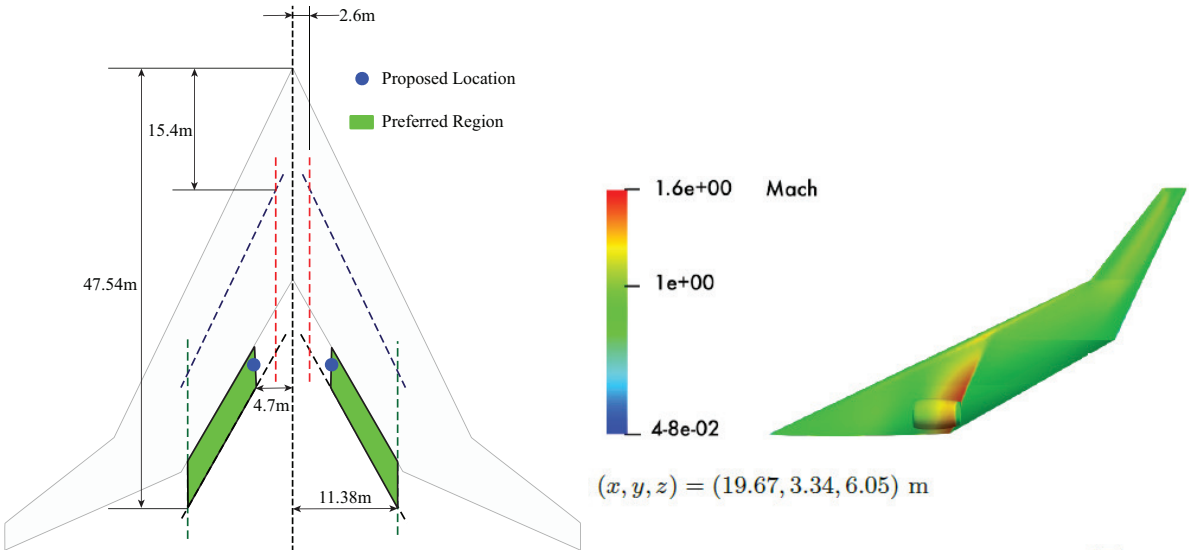

(a) Proposed Location

(b) Mach contours for an engine location showing supervelcoities

Fig. 2 Results from [8] for engine integration at h = 13 km, M_∞ = 0.85, and α = 2.9°

shockwaves as shown in Figure 2b. The study recommended a location (X = 37.38 m, Y = 4.70 m, and Z = 0.88 m) of the engine core. Based on the drag coefficient obtained for the isolated aircraft and the thrust provided by A350 engines, a thrust of 50 kN was assumed for each engine in this study. No specific engine sizing was conducted for this particular aircraft. Viscous effects were not considered, although they are crucial for comprehending the flow interaction between swept wing flow and the engine. A separate investigation is imperative to grasp boundary layer effects and their repercussions on engine inlet performance. More research about the aircraft's performance at off-design points and detailed studies on engine selection and sizing are required to proceed with engine integration.

Another research by [9] studied the 4.6% scaled model experimentally at low-speed conditions. The engine is located at X/L = 0.60 and $2Y/b$ = 0.16, and the experiment was performed in an open jet facility. At angles of attack more than 5°, interference drag is observed, with a maximum increase of 16.5% at 10°, while at lower angles, engine operation reduces drag. The highest interference drag penalty of 60 counts was at 10°. The interference effects on the lift and pitching moment are of the same order of magnitude as the installation effects due to thrust. This indicates that the thrust of the engine and the interaction between the engine and the wing must be considered in aerodynamic analysis. Therefore, the mutual interactions between the wing and engine must be understood in detail to ensure proper engine integration over the wing. The lift and pitching moment coefficients are amplified at high thrust settings, highlighting substantial distortions and interference effects that must be considered in aerodynamic design.

There is a significant lack of research on engine integration for flying wing aircraft with an over-the-wing engine configuration. Most aircraft that exhibit a flow pattern similar to the Flying V, such as the Blended Wing Body (BWB), are still in development, and literature on engine integration for such aircraft is not widely available in the public domain. As a result, a study is needed to understand the flow characteristics of these aircraft at both on-design and off-design conditions so that engine location and integration approaches can be systematically investigated.

This study addresses these gaps by conducting comprehensive aerodynamic analyses of the Flying V-1000 using RANS (Reynolds-averaged Navier-Stokes equations) at design and off-design points. The flow over the wing at these points would be thoroughly studied to understand the flow characteristics. This is crucial because the engine location, as discussed by [8], and integration approaches significantly affect inlet efficiency, aerodynamic performance, stability, and control. Additionally, this research will contribute to a deeper understanding of the Flying V's aerodynamic behavior and inform engine integration strategies. The study will examine boundary layers at various design points and report flow distortion, which will help identify the preferred region for the engine placement and integration approach.

As a preliminary step, engine sizing will be briefly addressed to establish the key dimensions required for this study. This step is imperative, as these dimensions will play a key role in evaluating flow distortions and determining suitable engine placement and integration strategies.

With the engine selection yet to be finalized, the thrust is computed using the thrust-to-weight ratio of the Airbus A350-1000, which is 0.27 [10]. This approach provides a baseline for estimating the dimensions of the engine. The MTOM of the Flying V-1000 is estimated at 266 tonnes, based on previous research by [10]. This results in a take-off thrust of 360 kN. Because the bypass ratio is unknown, the subsequent analysis shows how the fan diameter of the engine is selected.

Multiple engines are considered as reference engines for the Flying V and tabulated in Table 1. The most modern in-service engines have a bypass ratio of 10:1, while the under-development Ultrafan has a bypass ratio of 15:1.

Table 1 Engine specifications of reference engines.

Aircraft	Engine	Take-Off Thrust (kN)	Max. continuous Thrust (kN)	Fan Diameter (m)	BPR	Source
B 787	Trent 1000-R	360	323	2.85	10:1	[11]
A330-900	Trent 7000-72	324	289	2.85	10:1	[11]
A350-1000	Trent XWB-97	432	318	3.00	9.6:1	[12]
A350-900	Trent XWB-84	374		3.00	9.6:1	[12]
Boeing 777X	GE 9X	489	460	3.40	9.9:1	[13]
-	Ultrafan	112 - 490	-	3.56	15:1	[14]

To see the effect of the bypass ratio on the fan diameter, the Trent 1000-R and Ultrafan have each been used in the rubber engine sizing process. The last column of Table 2 shows the estimated fan diameter for the Flying V engine, when these engines are scaled to the required thrust for the Flying V. As can be seen, if a bypass ratio (BPR) of 10 is assumed, the estimated fan diameter would be 2.85 m, while with a bypass ratio of 15, the fan would measure 3.05 m in diameter. For this study, a tentative fan diameter of 3.00 m is being considered for the Flying V engine, considering that high-bypass-ratio engines are expected to become more common in the coming decade.

Table 2 Rubber engine sizing for a 360 kN turbofan engine of various bypass ratio (BPR).

Reference Engine	Fan diameter (m)	Thrust (kN)	BPR (-)	Scaling Factor (-)	Estimated diameter (m)
RR Trent 1000-R	2.85	360	10	1.00	2.85
RR Ultrafan	3.56	490	15	0.85	3.05

Having discussed the engine details, the study proceeds with a detailed methodology in Section II, which gives an overview of computational frameworks, numerical steps, and key parameters to be evaluated and discussed. In Section III, the results are presented in terms of aerodynamic performance, the vortex behavior at high angle-of-attack, the boundary layer state, and flow distortion at various engine locations. Finally, Section IV presents the conclusions of this study.

II. Methodology

This section discusses the dimensions and boundary conditions of the computational domains selected for the current study. Multiple grids have been generated, and their details are presented along with the grid independence study. The numerical setup, including the equations solved, is outlined. A test matrix has also been defined to facilitate the investigation by varying key parameters.

A. Computational Domain Grid Independence Study

The geometry for this study is developed in 3DExperience and exported to ICEM CFD to generate a computational domain and do meshing. Structured mesh generation focused on accurately capturing flow features while maintaining computational efficiency. Figure 3 shows the computational domain generated with its details. Figure 4a shows the 3D domain mesh, and Figure 4b shows the surface mesh and internal blocking on the Flying V.

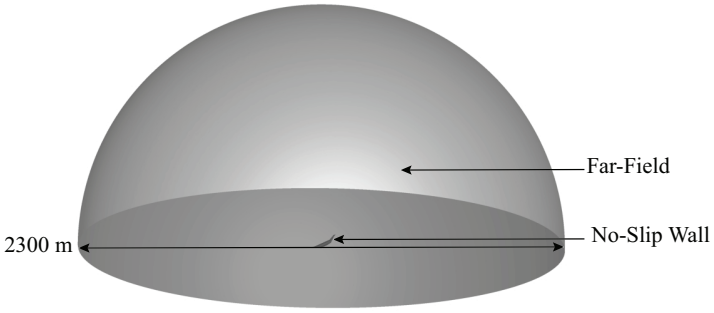

Fig. 3 Computational Domain

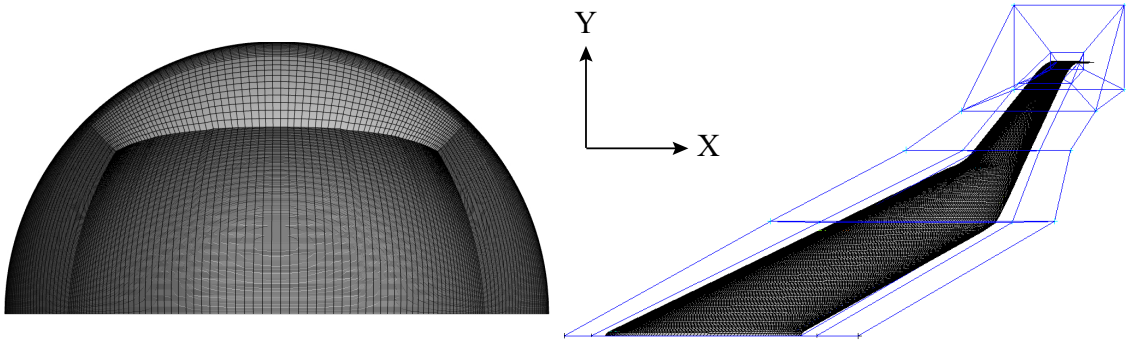

(a) 3D Mesh in the X-Y plane

(b) Surface mesh and internal blocking on Flying V

Fig. 4 Details of the computational mesh.

The grid employed in this study is selected after a mesh independence study. The characteristics of the tested grids are summarized in Table 3. Three meshes, labeled as Coarse, Medium, and Fine, are considered with a total number of cells, which doubles. Table 3 shows the number of elements on the airfoil along the span and the region close to the aircraft, labeled inner. The inner region extends along Z to a height of 50% of the local chord c. The height of the first dimensionless element y^+ is calculated at $M_\infty = 0.85$ for the aircraft. The height of the elements increases with an expansion ratio of 1.1. The far field is modeled as a semisphere with the symmetry plane coinciding with the aircraft symmetry plane. The nose of the aircraft is located at the center of the symmetry plane, and the semisphere has a radius of $120\overline{c}$.

Table 3 Number of cells and y^+ used for the mesh independence study of Flying V aircraft

	Airfoil	Span	y^+	Inner	Total cells (10^6)
Coarse	178	144	0.5	127	6.06
Medium*	224	182	0.4	156	12.1
Fine	280	229	0.3	200	24.1

Table 4 presents the results of a mesh independence study conducted at M_∞ of 0.2 and 0.85. For $M_\infty = 0.2$, the study considers $\alpha = 0°$, 10°, and 20°, while for $M_\infty = 0.85$, $\alpha = 0°$, 5°, and 10° are examined. The table provides the relative differences in C_D and C_L with respect to the extrapolated Richardson values as shown by [15], which are calculated as $\Delta C_L = C_L - C_{L,Richardson})/C_{L,Richardson}$ and similarly for ΔC_D. As expected, the relative differences decrease with increasing mesh refinement, confirming convergence. The medium mesh is selected for the present study based on these results.

Table 4 Mesh independence study at M_∞ = 0.2 and M_∞ = 0.85 at various α, Δ is the difference with respect to Richardson extrapolation value of C_D, C_L and C_M

	M_∞	α	ΔC_D	ΔC_L	M_∞	α	ΔC_D	ΔC_L
Coarse	0.2	0°	-7.9%	-19.6%	0.85	0°	-28.2%	-31.2%
	0.2	10°	2.5%	-4.6%	0.85	5°	-18.0%	-4.9%
	0.2	20°	9.1%	-0.73%	0.85	10°	1.1%	-4.5%
Medium	0.2	0°	-2.7%	-9.9%	0.85	0°	-10.2%	-13.7%
	0.2	10°	0.1%	-1.9%	0.85	5°	-5.0%	-1.1%
	0.2	20°	6.1%	-0.005%	0.85	10°	1.13%	-0.37%
Fine	0.2	0°	-0.07%	-1.1%	0.85	0°	-1.3%	-2.3%
	0.2	10°	0.01%	-0.04%	0.85	5°	-0.29%	-0.01%
	0.2	20°	0.32%	-0.002%	0.85	10°	0.01%	-0.001%

B. Numerical Simulation Setup

The study employs a finite volume method (FVM) solver to solve the Reynolds-Averaged Navier-Stokes (RANS) equations. RANS simulations decompose turbulent flows into time-averaged and fluctuating components. The turbulence model used is the k-ω Shear Stress Transport (k-ω SST) model, as validated by [16, 17], which has been shown to effectively capture complex turbulent behaviors, including boundary layer flows and separation. The solver uses a density-based approach with an implicit formulation and the Monotonic Upstream-centered Scheme for Conservation Laws (MUSCL) for spatial discretization. A least-squares cell-based method with a third-order MUSCL scheme minimizes numerical diffusion, ensuring accurate resolution of sharp gradients and turbulent features such as Turbulent Kinetic Energy (TKE) and the Dissipation Rate (ϵ).

This combination of the k-ω SST turbulence model, density-based solver, and advanced spatial discretization enables reliable simulations of compressible flows, including turbulent boundary layers. Residual targets of 10^{-5} are applied to the continuity, momentum, energy, k, and ω equations, ensuring robust convergence and high accuracy, particularly in flows with strong shocks and turbulence interactions.

C. Test Matrix

The operating conditions and the prospective engine locations have determined the test matrix. Figure 5(a) presents a three-dimensional visualization of the engine locations. The schematic shows only the engine location on the aircraft's

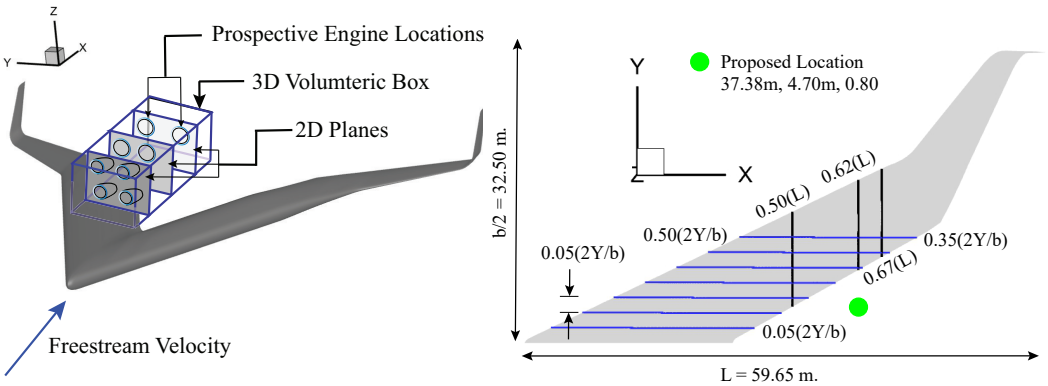

(a) Slices for computing inlet distortion of the Flying V

(b) Flying V depicting the slice locations

Fig. 5 Schematic depiction illustrating planes for engine integration locations and the slices considered for boundary layer and distortion assessment.

starboard side to ensure visual clarity. Figure 5(b) provides a schematic representation of the engine locations from a top view. Slices parallel to the wing root (in blue color) have been extracted to understand the boundary layer behavior of the Flying V configuration. Slices perpendicular to the streamwise location in the X-direction (in black color) have been extracted to understand the distortions in the flow. The proposed location by [8] is (X = 37.38 m, Y = 4.70 m, and Z = 0.88 m) from the engine core is also shown in Figure 5b.

Table 5 presents the operating conditions for three flight phases: takeoff, climb, and cruise. It includes the mean aerodynamic chord-based Reynolds numbers and Mach numbers at various altitudes. The effects of the Reynolds number are not expected to be significant, as the lowest Reynolds numbers are on the order of 10×10^6. Therefore, a Reynolds number of 100×10^6 has been chosen to isolate and study the effects of Mach number.

Table 5 Operating conditions of Flying V with $\overline{c}$ being the mean aerodynamic chord (MAC): $\overline{c}$ = 18m.

S. No.	Flight Phase	h (m)	M_∞ (~)	$Re_{\overline{c}}$ (10^6)
01	Take-Off	0	0.2	84
02	Take-Off	0	0.25	105
03	Take-Off	0	0.3	126
05	Climb	3250	0.40	124
06	Climb	4875	0.47	124
07	Climb	6500	0.55	123
08	Climb	9750	0.70	110
09	Cruise	13000	0.85	83.4
10	Dive	13000	0.99	97.3

The study will investigate the aerodynamic performance of the Flying V, focusing on lift, drag, and pitching moment coefficients across various Mach numbers. Moreover, building on the location proposed by [8], it will analyze the surrounding region to examine the flow physics over the suction surface and wake. This detailed analysis aims to provide critical insights into the engine integration location and its approach.

III. Results and Discussions

This section discusses the aerodynamics of flying V at design and off-design conditions. Mach number effects have been reported for $Re_{\overline{c}} = 100 \times 10^6$. Vortex behavior over the wing at high angles of attack for low Mach numbers has been analyzed and discussed. Boundary layer profiles for various locations and surface streamlines on the wing have been presented. Based on these profiles, engine location and integration approaches have been discussed. Engine sizing has been done, and distortion in flow over wing and wake has been discussed to propose a preferred region where the engine can be placed with minimal distortions.

A. Aerodynamic Performance in Flight Envelope

This section delves into the aerodynamic performance of the Flying V for various Mach numbers. The aerodynamic characteristics of the Flying V have been quantitatively analyzed by evaluating the lift coefficient C_L, drag coefficient C_D, and pitching moment coefficient C_M across a range of angles of attack α and is depicted in Figure 6.

M_∞ = 0.2, 0.25, and 0.3 have been simulated at sea level conditions attempting to replicate the take-off and approach conditions. The Mach effects here are negligible because of the minimal compressibility effects. At high angles of attack, changes in C_D can be attributed to the dynamic and unsteady nature of the three-dimensional flow with complex vortex systems, posing significant challenges in accurately modeling these effects using RANS. The decrease in the aerodynamic performance (C_L/C_D) in Figure 6c mainly results from the increased flow separation in the outer wing discussed by [18] and also due to trailing edge vortices. At higher speed, for M_∞ = 0.65, 0.75, and 0.85, the Mach number effects lead to an increase in drag, resulting in a decrease in C_L/C_D at higher angles of attack. This increase in drag force occurs because of the trailing edge vortex generation.

The pitching moment coefficient in Figure 6d has been computed by considering the moment reference point (MRP) at the most forward C_G location. With the increasing Mach number, the pitching moment coefficient, also known as

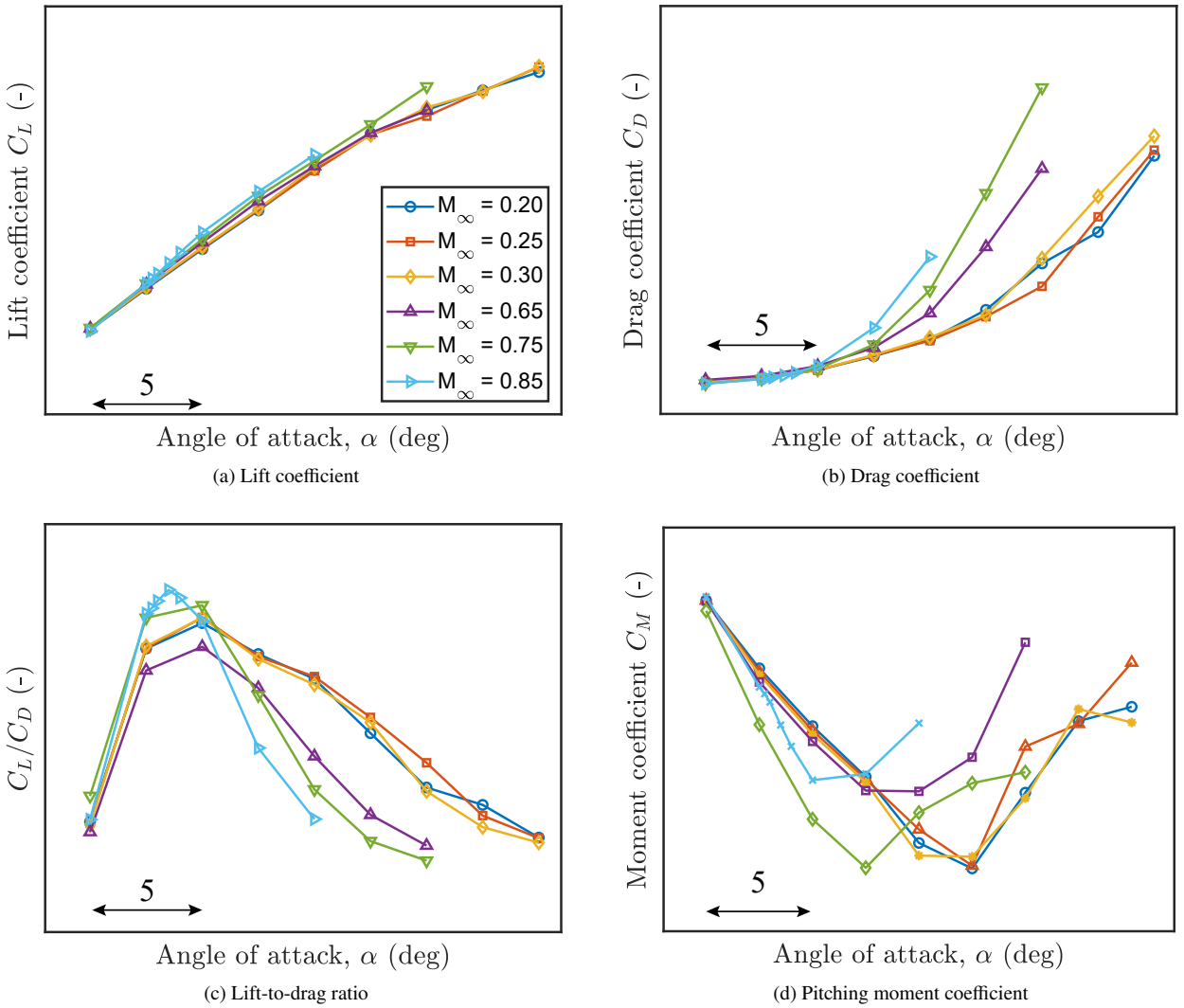

(a) Lift coefficient

(b) Drag coefficient

(c) Lift-to-drag ratio

(d) Pitching moment coefficient

Fig. 6 Aerodynamic coefficients as a function of α at various M_∞ at $Re_{\bar{c}} = 100 \times 10^6$.

pitch break, starts occurring at lower angles of attack. This can also be seen as the change in slope of the lift coefficient curve in Figure 6a. The pitch break phenomena and changing this angle of attack have been discussed in detail by [18]. To gain a deeper understanding of the trends in lift, drag, and moment coefficients, the flow over the wing is analyzed in detail in the following section, with a focus on various locations along the wing. Vortex behavior at different angles of attack, along with pressure distribution over the wing, is also thoroughly discussed and examined.

B. Vortex Behavior and Pressure Distribution at Takeoff and Cruise Conditions

Highly swept wings generate vortices at high angles of attack, often leading to complex interactions and occasional vortex bursting. These dynamics significantly influence aerodynamic performance. Vortex behavior at $M_\infty = 0.25$ is discussed at $\alpha = 12.5°, 17.5°$. For cruise condition at $M\infty = 0.85$, vortex behavior is discussed at $\alpha = 3°$.

Figure 7 shows non-dimensional axial-vorticity at various streamwise locations ($X/L = 0.41$, $X/L = 0.5$, $X/L = 0.62$) at $\alpha = 12.5°$, and $\alpha = 17.5°$. The vortex generation increases towards the outer wing, which can be seen at $X/L = 0.62$. These vortices are caused due to the increasing spanwise velocity along the trailing edge, accentuating and forming a vortex. At $\alpha = 12.5°$, for X/L = 0.41, no well-defined vortex core is there, but a rotational behavior does exist in the flow as depicted by the vorticity contours. The vortex core is present at X/L = 0.50, located before $X/c_{\text{Local}} = 0.5$, which becomes more pronounced at X/L = 0.62. The vortex core is located after $X/c_{\text{Local}} = 0.5$ and is detached from

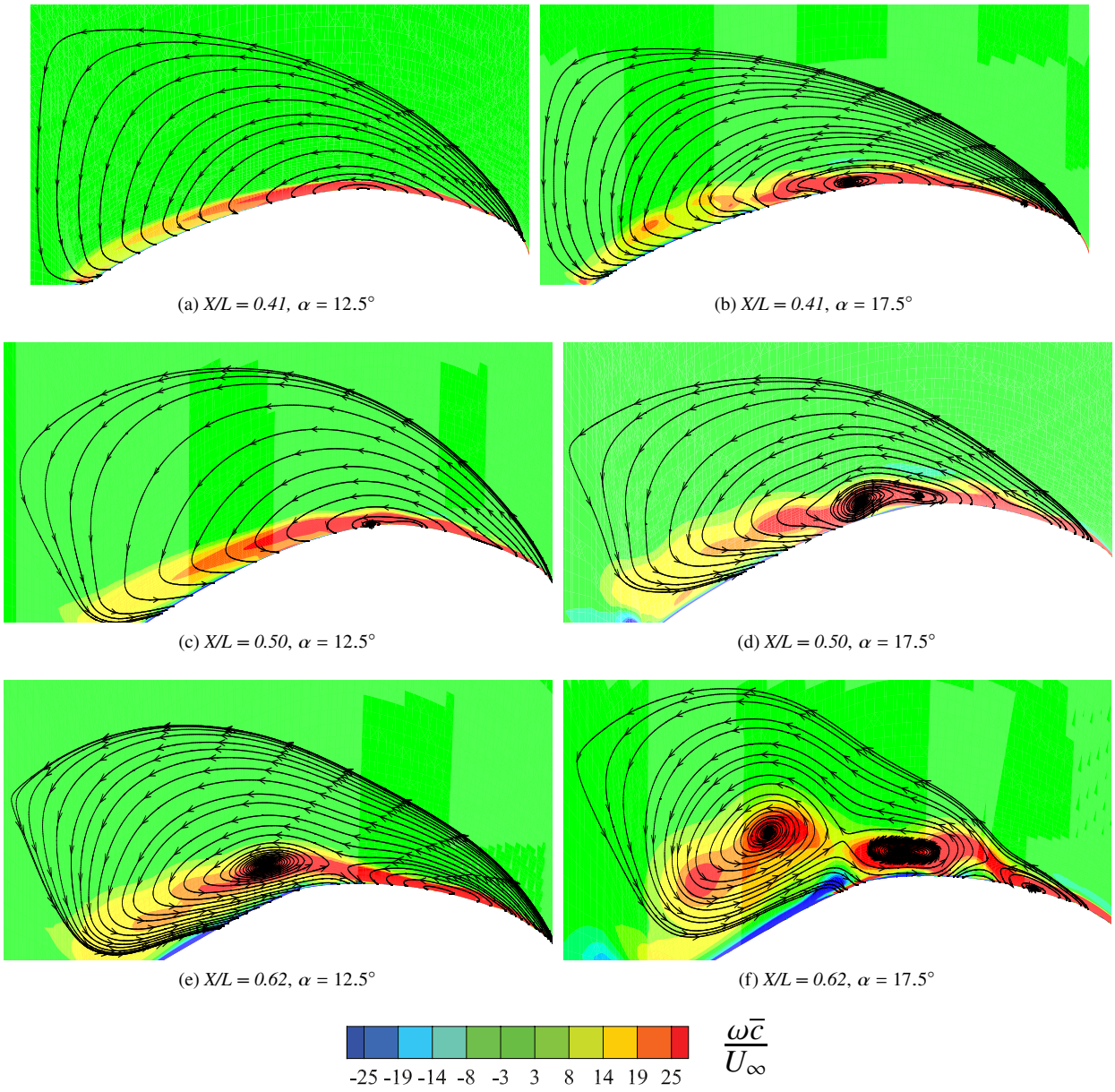

(a) *X/L = 0.41*, α = 12.5°

(b) *X/L = 0.41*, α = 17.5°

(c) *X/L = 0.50*, α = 12.5°

(d) *X/L = 0.50*, α = 17.5°

(e) *X/L = 0.62*, α = 12.5°

(f) *X/L = 0.62*, α = 17.5°

Fig. 7 Non-dimensional axial vorticity at various locations in streamwise direction at $M_\infty = 0.25$ (These images are not to scale)

the wing surface. Another small vortex is developed before $X/c_{\text{Local}} = 0.5$. When α = 17.5°, at X/L = 0.41, a vortex at $X/c_{\text{Local}} \approx 0.5$ is observed, which then becomes pronounced at X/L = 0.50 and tends to breakdown. At X/L = 0.62, that vortex has disintegrated into two vortices, and a small vortex is also observed before $X/c_{\text{Local}} = 0.5$.

Non-dimensional axial vorticity for various slices over the Flying V has been shown in Figure 8 at α = 12.5°, and 17.5° in low speeds conditions. At α = 12.5° trailing edge vortex (TEV) is developed and moves towards the outboard wing. The TEV detaches from the shear layer, generating an inboard vortex (IBV) before the trailing edge kink. The TEV detaches from the trailing edge kink into a burst area, and the IBV disintegrates into two vortices in the outboard wing. Since the local chord in the outboard wing becomes quite small, abrupt vortex detachments can be seen. At higher angles of attack of α = 17.5°, the TEV is much more pronounced and detaches at the trailing edge kink. The IBV generation occurs much earlier than at lower angles of attack. The figure shows four and five vortices detaching from the

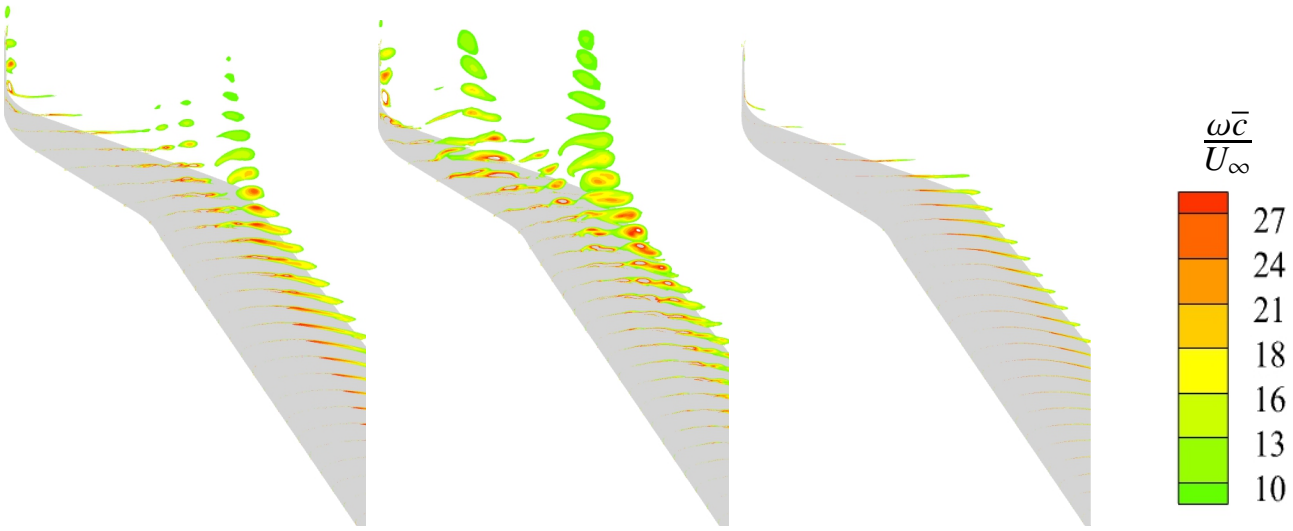

(a) $\alpha = 12.5°$, $M_\infty = 0.25$ (b) $\alpha = 17.5°$, $M_\infty = 0.25$ (c) $\alpha = 3°$, $M_\infty = 0.85$

Fig. 8 Non-dimensional axial vorticity distribution for various α, and M_∞(These images are not to scale)

wing surface, including the wingtip vortex for $\alpha = 12.5°$ and $17.5°$ respectively.

The vortex behavior, as discussed, is notably complex, with new vortices forming, detaching from the surface, and eventually shedding from the wing at the trailing edge. To complement this understanding, examining the complete pressure distribution would provide valuable insights into the overall pressure variations across the surface. The aircraft's surface streamlines and pressure coefficient (C_p) distributions provide valuable insights into the flow behavior near the surface and its impact on aerodynamic performance. These analyses are essential for determining the optimal engine placement, ensuring minimal disruption to lift generation, maintaining a uniform flow intake for engine efficiency, and leveraging beneficial flow interactions.

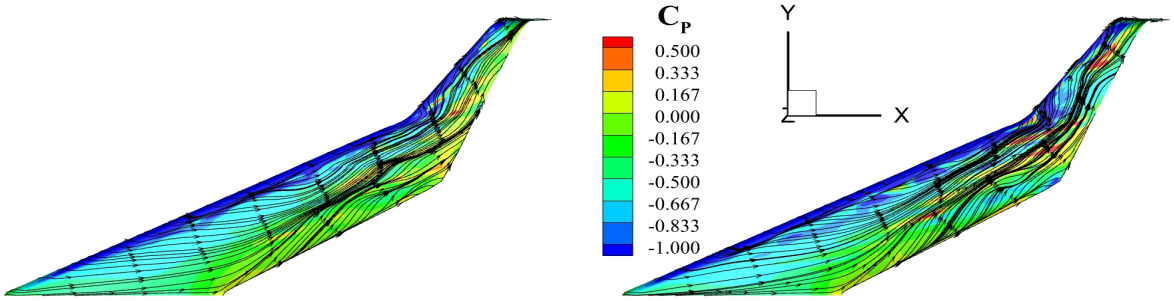

(a) $\alpha = 15°$, $M_\infty = 0.25$ (b) $\alpha = 17.5°$, $M_\infty = 0.25$

Fig. 9 Pressure coefficient (C_P) and shear stress surface streamlines (These images are not to scale)

Figure 9 shows the coefficient of pressure distribution and the streamlines on the aircraft at α and M_∞, which are the main focus of this study. Figure 9a feature $M_\infty = 0.25$ and $\alpha = 15°$, Figure 9b $M_\infty = 0.25$ and $\alpha = 17.5°$.Different M_∞ are considered; however, the flow changes here depend on α as described in [18]. At a low angle of attack, as in Figure 9a, the streamlines show the presence of crossflow in the trailing edge area of the inner wing. When increasing α, the crossflow reaches the outer wing, extending up to the leading edge as in Figure 9b, forming two vortices in the trailing edge area of the inner wing. The typical S-shape of the streamlines represents the vortex presence. Further, an increase in α, as in Figure 9b, leads the main vortices to move more upstream and the smaller one to detach from the wing and not be visible in the streamlines. The C_P near is higher for some regions at $\alpha = 17.5°$ compared to $\alpha = 15°$. These are generally in regions where the vortex detaches from the wing surface (loses connection to the surface). The

trailing edge vortex detaching and leaving the wing surface can be visualized in Figure 8. The vortices on the wing help generate lift as they create a suction peak (lower static pressure). This has been quantitatively discussed in [18].

Now, after analyzing the flow behavior and the presence of vortices in this section, engine integration can be performed on the wing surface or in the wake region using various approaches. The following subsections will discuss the boundary layer behavior using boundary layer profiles to evaluate the location and approach of engine integration on the wing surface. Additionally, the wake region will be examined to assess flow distortions both over the wing and within the wake to evaluate the engine integration location and approach.

C. Boundary Layer Behavior at Takeoff and Cruise Conditions

Engine integration can follow two main approaches: podded and buried configurations. In a buried engine, the engine is partially embedded in the airframe, which reduces drag due to the smaller wetted surface area. However, it experiences lower inlet pressure recovery because it ingests air from the slower-moving boundary layer. In contrast, a podded engine is mounted on a pylon outside the boundary layer, allowing it to take in uniform intake flow, resulting in better pressure recovery. We can determine the best engine location and integration approach by understanding how the boundary layer behaves during different flight conditions, such as takeoff and cruise at various locations.

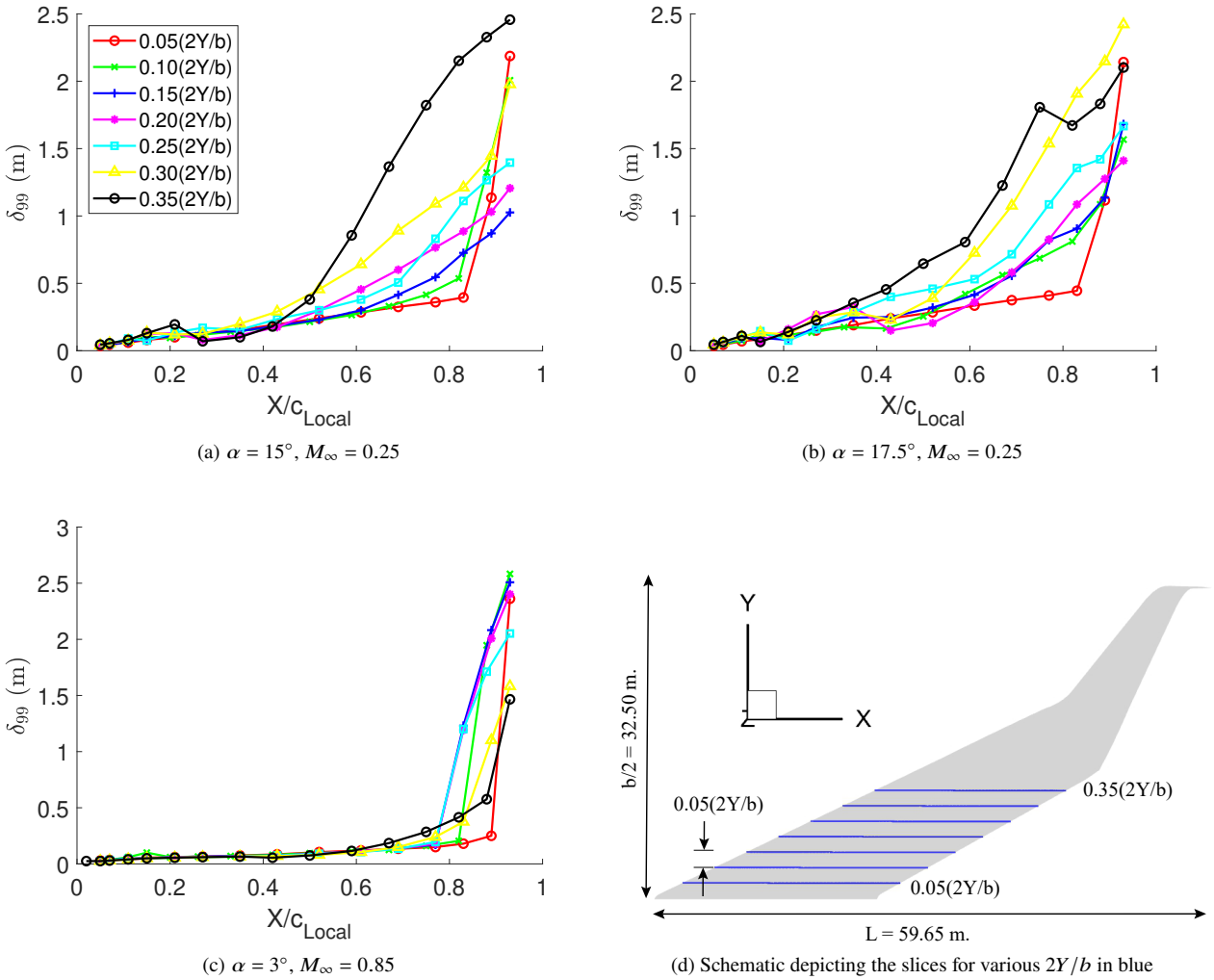

(a) $\alpha = 15°$, $M_\infty = 0.25$

(b) $\alpha = 17.5°$, $M_\infty = 0.25$

(c) $\alpha = 3°$, $M_\infty = 0.85$

(d) Schematic depicting the slices for various $2Y/b$ in blue

Fig. 10 δ_{99} for various α at $M_\infty = 0.25$.

Figure 10 presents the boundary layer thickness, δ_{99}, for two different α under takeoff and at one α at cruise conditions. The data were obtained by taking slices parallel to the wing root at various $2Y/b$ locations along the span as

depicted in Figure 10d. The X/C_{Local} on the X axis is for these airfoils parallel to the wing root. All slices were taken before the trailing edge kink to ensure a consistent analysis. Only the U component has been considered for calculating δ_{99}. This approach is chosen to isolate the streamwise flow velocity, U, since an idealized scenario would expect a uniform streamwise velocity of $U = 100\%$ at engine highlight, corresponding to the highest inlet pressure recovery in the flow. Focusing exclusively on U makes the analysis more straightforward, allowing a better understanding of the axial flow the engine would face during operation.

At $M_\infty = 0.25$, the boundary layer at $\alpha = 15°$ increases near the trailing edge and towards the outboard wing. At lower $2Y/b$, the boundary layer develops gradually due to the natural deceleration of the flow and turbulent mixing. Near the trailing edge, the trend becomes steep as the adverse pressure gradient causes the boundary layer to thicken more rapidly. At higher $2Y/b$, the U component decreases, and the trailing edge is mainly dominated by the V component, which is depicted through a steeper increase in δ_{99} at $\alpha = 17.5°$. For both $\alpha = 15°$ and $17.5°$, vortices are present on the wing as depicted in Figure 8. These vortices induce a local turbulent mixing, increasing the boundary layer thickness, which would have caused the fluctuations shown in Figure 10. The boundary layer development for all the $2Y/b$ locations at $\alpha = 15°$ show slight change till $X/c_{\text{Local}} < 0.4$. This phenomenon occurs at lower X/c_{Local} for $\alpha = 17.5°$ due to multiple vortices leading to enhanced mixing in the boundary layer. At higher angles of attack, the U decreases much more drastically along the span, leading to a sharper increase in δ_{99}. At the design point of $M_\infty = 0.85$, the growth of the boundary layer is very gradual till $X/c_{\text{Local}} < 0.75$ for all $2Y/b$. The adverse pressure gradients and a strong spanwise velocity component lead to a sharp increase in δ_{99} near the trailing edge.

The podded engine integration, if considered, should be kept outside the boundary layer because, at the off-design points like takeoff, where the aircraft is at higher angles of attack, the engine would face a highly distorted flow, decreasing the inlet pressure recovery. A recommended engine location from previous research by [8] is at $2Y/b = 0.14$ behind the trailing edge. In the Figure, the blue line depicts $2Y/b = 0.15$ closest chordwise location. δ_{99} for $2Y/b = 0.15$ is between 0.8 - 1.25 at $M_\infty = 0.25$. At $M_\infty = 0.85$, the δ_{99} profile appears more favorable; however, low-speed operating conditions impose constraints on engine placement, as the takeoff mass flow capture ratio must be ≈ 2.0. A non-uniform, distorted flow—particularly as one moves toward the trailing edge and outboard sections of the wing—poses challenges to engine inlet performance by reducing flow uniformity and increasing susceptibility to distortion effects. For buried integration configuration, the preferred region of engine location should be $2Y/b < 0.20$ and $X/c_{\text{Local}} < 0.6$. An active flow control device near the inlet must be employed to mitigate flow distortion. For podded engine integration, it is crucial to investigate the wake of the Flying V to identify regions where flow distortion decreases to a level that allows the engine to face a sufficiently uniform flow.

D. Flow Distortion at Engine Locations

Engine inlet performance is crucial in determining the propulsive efficiency of the engine. Two critical metrics for engine inlet performance are inlet distortion and inlet pressure recovery. This study examines flow over the wing and the wake to understand and quantify distortion. The effects of engine placement over the wing are particularly interesting, as they directly influence engine efficiency and the overall aircraft performance. Quantifying flow distortion at the engine inlet is essential, and parameters such as the total pressure at the nacelle lip and the aerodynamic interface plane (AIP) are critical in this analysis. One widely used metric for this purpose is the distortion coefficient (DC_θ), defined as:

$$\text{DC}_\theta = \frac{p_{\text{t},avg} - p_{\theta,\text{t},min}}{\frac{1}{2}\rho V_\infty^2}$$

where $p_{\text{t},avg}$ is the average total pressure across all sectors, $p_{\theta,\text{t},min}$ is the average total pressure in the sector with the minimum total pressure, $\frac{1}{2}\rho V_\infty^2$ is the dynamic pressure, and θ is angle of each sector angle. This metric represents the extent of pressure variation within the inlet flow, with higher values indicating more significant distortion and potential performance degradation. Understanding DC_θ is vital for assessing the aerodynamic impact of different engine placement configurations.

Table 6 Distortion coefficient (DC_{60}) at recommended location by Ref. [8]

flow condition:	$\alpha = 15°$, $M_\infty = 0.25$	$\alpha = 17.5°$, $M_\infty = 0.25$	$\alpha = 3°$, $M_\infty = 0.85$
DC_{60}	0.0374	0.0227	0.0403

The plots in Figure 11 show the non-dimensional streamwise velocity near the recommended location ($X = 37.4$ m, $Y = 4.7$ m, $Z = 0.8$ m) by [8]. This research was done through Euler simulations at $M_\infty = 0.85$. The distortions

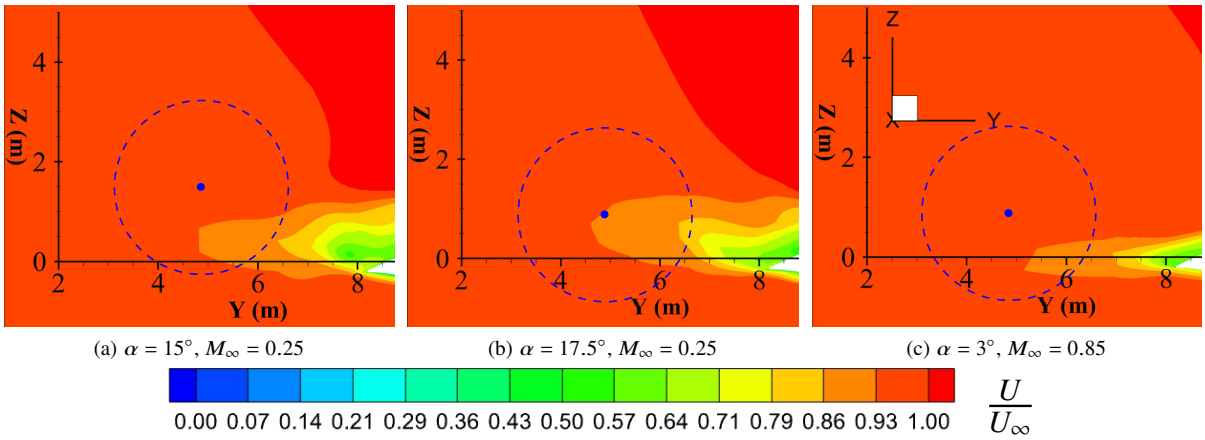

(a) $\alpha = 15°$, $M_\infty = 0.25$ (b) $\alpha = 17.5°$, $M_\infty = 0.25$ (c) $\alpha = 3°$, $M_\infty = 0.85$

Fig. 11 Non-dimensional streamwise velocity at the proposed location by [8] with the circle depicting the flow engine inlet will face.

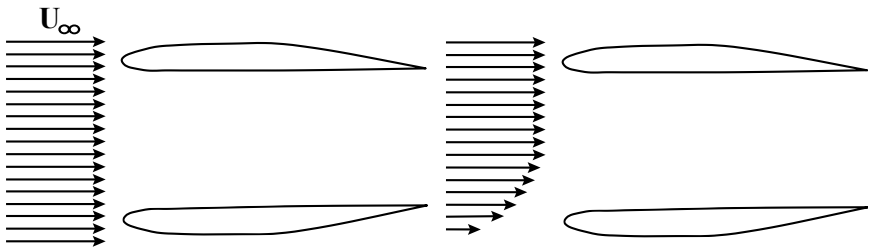

Fig. 12 A schematic showing the comparison of ideal uniform and non-uniform flow intakes.

have been presented for this location in Table 6 for low and high-speed conditions. The distortions are high at cruise as well as at low-speed conditions. At an angle of attack of $\alpha = 15°$, the lowest pressure region is concentrated in a small area. However, at a higher angle of attack, $\alpha = 17.5°$, the low-pressure region becomes more distributed. Significant distortions have been observed at low and high speeds for this engine configuration, exceeding 4% at $\alpha = 3°$ for $M_\infty = 0.85$. This would be much higher at the aerodynamic interface plane (AIP) with the engine. Euler simulations do not account for viscosity, which is essential for modeling boundary layers and wake formation, leading to inaccurate drag representation. As a result, the lift-to-drag ratio, presented by [8], is not completely correct because the drag component, particularly from wake and boundary layer separation, is not adequately captured.

In Figure 11a, the intake flow is non-uniform, with the U decreasing due to the trailing edge wake. A small region with a lower U can be seen. This decreased U is present in a larger region at a higher $\alpha = 17.5°$ in Figure 11b. Even at cruise conditions, there is a non-uniformity in flow. The intake flow will have low velocity in the lower region of the engine. This distorted flow can be considered a low-velocity flow being ingested. A 2-D schematic shown in Figure 12 illustrates how the flow enters the engine when there is a lower velocity in the intake flow. The figure on the left shows the ideal flow with uniform U, while the right shows a non-uniform intake flow. When an engine is exposed to nonuniform flow, it experiences significant inlet distortions, which lead to a reduction in pressure recovery. Therefore, the engine location recommended by [8] would not be favorable from an inlet efficiency point of view.

Because of this, a detailed examination of the wake is required to determine the optimal location for the engine. In the current study, no engine has been placed on the aircraft. However, a preliminary investigation is conducted to assess distortion levels at potential engine locations. The flow behavior over the wing and the wake behind the trailing edge is analyzed to identify the optimal installation location by quantifying the distortions in flow. A circular region representing engine highlight at the inlet is analyzed by dividing it into six 60° sectors.The region of interest, as defined by [8], has been expanded to provide greater flexibility and a broader understanding of the flow field. Figure 13 shows how the sectors were considered for an engine inlet to compute distortions along with their DC_{60}.

The Distortion Coefficient DC_{60} is computed at several potential engine locations as shown in Figures 14 and 15.

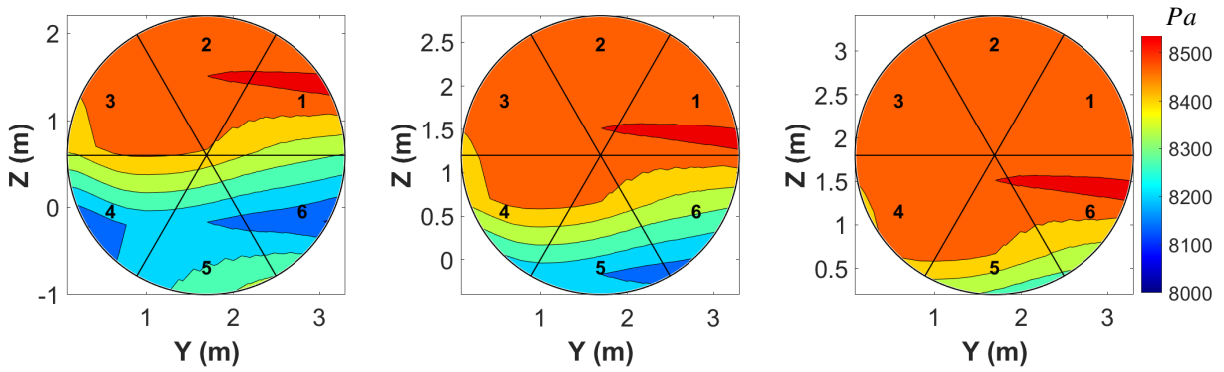

(a) Y = 1.69m, Z = 0.60m, DC_{60} = 1.8% (b) Y = 1.69m, Z = 1.20m, DC_{60} = 1.9% (c) Y = 1.69m, Z = 1.80m, DC_{60} = 0.6%

Fig. 13 Total pressure (p_t) at $\alpha = 3°$ at M_∞ = 0.85 for various engine locations.

Three slices at *X/L* = 0.50, 0.62, and 0.67 were analyzed, defining potential locations in the spanwise and vertical directions within the region of interest. In Figure 13, the center of the circle represents the engine core, with a radius of 1.6 meters. The radius chosen for the calculations provided an initial estimate of the distortion levels at various potential locations. A grid is created for each slice where most of the engine locations were placed at lower values of Z as the distortion levels decreased with increasing distance in the Z direction. This process is carried out in three phases. Initially, a uniform grid is considered, followed by two additional phases in which more engine locations were selected based on changes in the DC_{60} values. At $\alpha = 17.5°$ for $M_\infty = 0.25$, the distortion increases towards the span-wise direction $2Y/b$ at all the streamwise locations as shown in Figure 14. At $\alpha = 17.5°$, significant distortion is observed at $X/L = 0.50$. This distortion is primarily attributed to the trailing edge wake at lower $2Y/b$ and the increased thickness of the wing root, which exacerbate flow disruptions in this region. At $X/L = 0.62$, and 0.67, the DC_{60} values show an increase in distortion with increasing $2Y/b$. This is mainly due to the increased V along the trailing edge. The distortion decreases significantly beyond 6m in the vertical direction at all the *X/L*.

Figure 15 shows the distortion at various *X/L* locations for $\alpha = 3°$. The distortion is very low in cruise conditions compared to takeoff operating conditions. Here, there is much more freedom in choosing the engine location. Still, takeoff conditions will also be crucial in determining the engine location as the engine is functional at the highest thrust rating during takeoff. A distorted flow will be detrimental to the engine blades, decreasing the inlet pressure recovery and potentially leading to compressor surge.

An engine over the wing with a higher distance in a vertical direction would be ideal. The intake flow would have negligible distortions, but a much larger pylon would be needed, increasing the wetted area and leading to a higher skin friction drag. The space between the wing and the engine would generate supervelocities, which would result in degradation in aerodynamic performance as highlighted by [8]. From a maintenance perspective, dismounting the engine without an external crane must also be factored in, which would give rise to another set of problems.

The aircraft's wake region, extending from 30–38 m in the X direction, 5 m in the Y direction, and beyond 5 m in the Z vertically is the most favorable location for engine placement, balancing aerodynamic, structural, and safety considerations. A lower *2Y/b* presents safety challenges, such as an increased risk in an event of a turbine disk failure. At the same time, a higher *X/L* introduces complications in flight dynamics, mainly when using the rudder. The center of gravity (CG) is aligned with the root chord. At a higher *X/L*, the resultant moment arm would be longer, increasing the demands on control surfaces and making it difficult to trim the aircraft effectively. A convergent-divergent channel could also form between nacelles at lower $2Y/b$, leading to excessive supervelocities.

Higher values of Y than 5 m would significantly impact the rudders located on the aircraft winglet. Offline handling qualities simulations [19] conducted for the one engine out case, with an engine located at Y=4.7 m, shows that bigger winglets are required to accommodate the rudder, which can satisfy the requirements at different flight conditions. The distance along Y is higher than proposed here, but the values of thrust considered are determined only from level flight, being at most T/W = 0.11, which is 40% of the T/W considered in this study. If the engine is located above the CG, the thrust also impacts the pitching moment and, hence, the requirements for the elevator.

The flow physics over the wing strongly influences engine location, particularly at high angles of attack, where

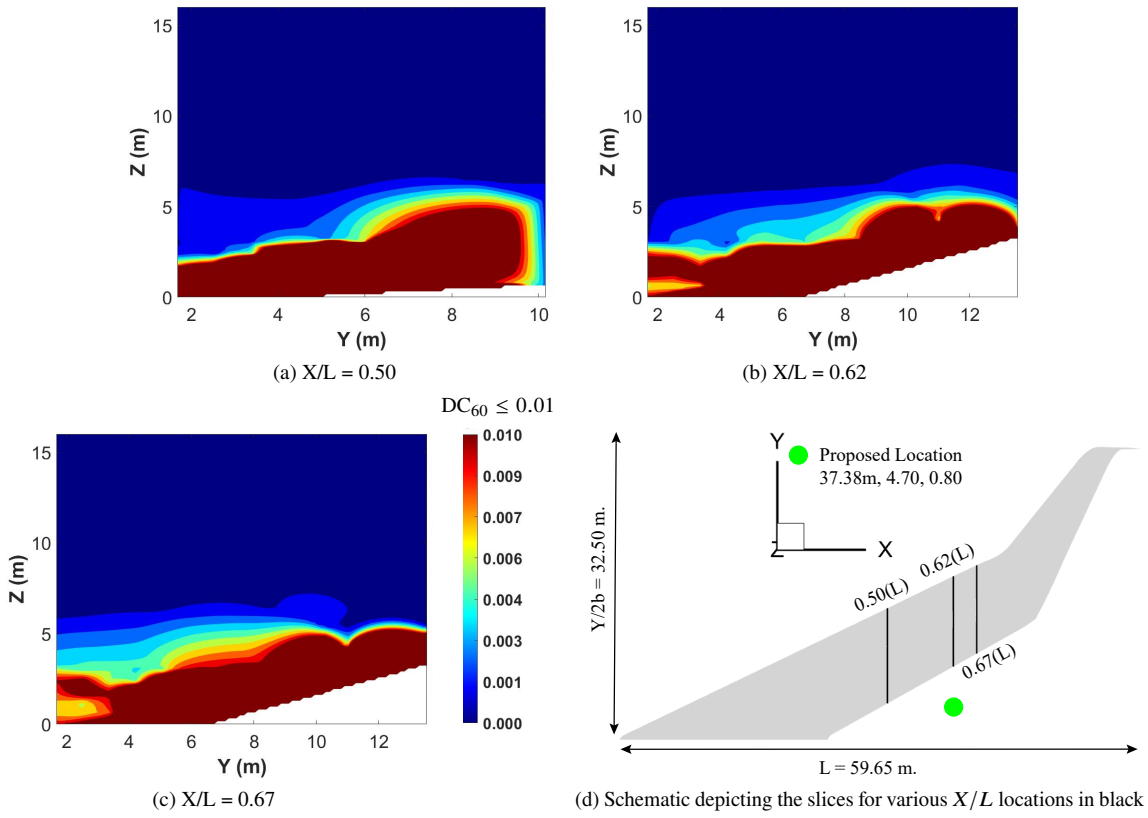

(a) X/L = 0.50 (b) X/L = 0.62

(c) X/L = 0.67 (d) Schematic depicting the slices for various X/L locations in black

Fig. 14 Distortion coefficient (DC_{60}) at $\alpha = 17.5°$ at M_∞ = 0.25.

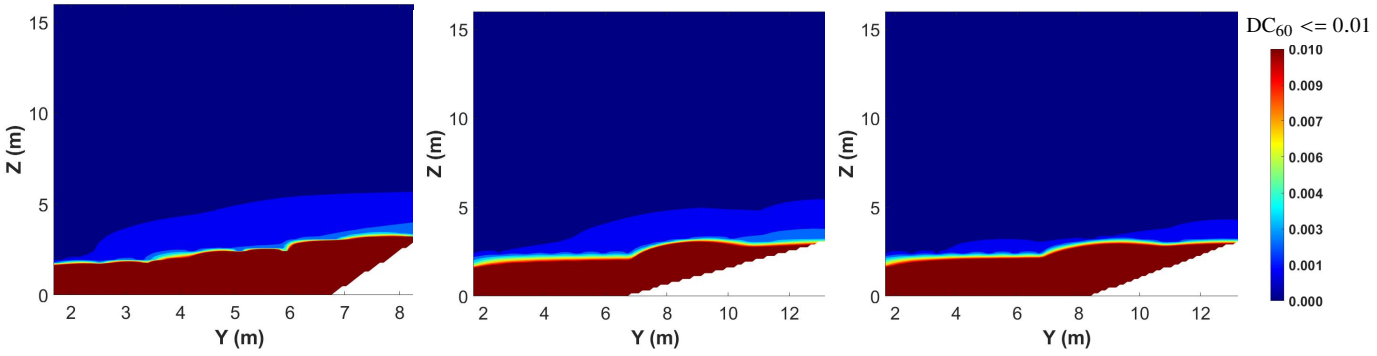

(a) X/L = 0.50 (b) X/L = 0.62 (c) X/L = 0.67

Fig. 15 Distortion coefficient (DC_{60}) at $\alpha = 3°$ at M_∞ = 0.85.

trailing-edge vortices become prominent. These vortices, coupled with the required engines' high mass flow capture ratio (MFCR) nearing 2, restrict the streamwise positioning of the engines. Locating the engines within the wake region mitigates the adverse effects of vortices during low-speed flight while maintaining effective aerodynamic control. Ensuring a uniform inlet velocity profile is critical for achieving high inlet pressure recovery, and this region provides favorable conditions by minimizing distortion coefficients. Vertical placement reduces distortion by positioning the engine outside the boundary layer, improving inflow uniformity and performance stability.

IV. Conclusions

The aerodynamic performance of the Flying V has been numerically analyzed to identify an optimal region for engine placement under both on-design and off-design conditions. The simulations were conducted using Reynolds-Averaged Navier-Stokes (RANS) equations at $Re_{\text{MAC}} = 100 \times 10^6$ for various Mach numbers, capturing detailed insights into the flow physics and their implications on engine integration. Lift, drag, and moment coefficients were analyzed for various Mach numbers. Vortex behavior, boundary layer characteristics, and surface streamlines were discussed in detail. Engine sizing and flow distortion analysis were used to determine the preferred region for integration and its approach.

No stall has been observed for all Mach numbers. The drag coefficient increases as the trailing edge vortices start generating at higher angles of attack. The aerodynamic performance (C_L/C_D) for cruise conditions is consistent with the previous studies. At $M_\infty = 0.25$, vortices are observed at high angles of attack, which disintegrate into multiple small vortices moving towards the outer wing and upstream. Two and three vortices have been seen at 50% and 63% of L respectively at $\alpha = 17.5°$. δ_{99} exhibits minimal change up to $X/C_{\text{Local}} = 0.4$ for $\alpha = 15°$ at low Mach numbers and up to $X/C_{\text{Local}} = 0.75$ at high Mach numbers. Engine sizing was done to predict the thrust required for takeoff for Flying V-1000, and the thrust required was 360kN for one engine. Distortion at the location recommended by previous research shows high DC_{60} values between 2% and 4%. For podded engine integration, the wake region from 50% to 64% of L, $\approx$ 15% of semi-span($b/2$), and beyond 33% of $\overline{c}$ in Z direction was determined based upon the DC_{60} values. For buried engine integration, the preferred region lies within 20% of semi-span ($b/2$). A flow control device will be needed to handle the engine inlet distortion.

Numerical simulations at on-design and off-design conditions are essential for evaluating a podded engine integration within the proposed engine location region, as the DC_{60} values are expected to be significantly higher when computed at the Aerodynamic Interface Plane (AIP). Additionally, experimental analysis would be invaluable in validating the ability of podded engine integration simulation to capture key flow features accurately. This is particularly important as RANS simulations can become unreliable when predicting highly complex flow phenomena, necessitating experimental verification to ensure the fidelity of the numerical predictions.

V. Acknowledgments

The authors would like to acknowledge Nikki van Luijk for helping with the internal review and suggestions for the manuscript. Furthermore, the authors would like to thank the rest of the Flying V team for their help and insights during the research.

References

[1] Rosales Calderon, O., Tao, L., Abdullah, Z., Moriarty, K., Smolinski, S., Milbrandt, A., Talmadge, M., et al., "Sustainable Aviation Fuel (SAF) State-of-Industry Report: State of SAF Production Process," Technical Report NREL/TP-5100-87802, National Renewable Energy Laboratory, Golden, CO, 2024. URL `https://www.nrel.gov/docs/fy24osti/87802.pdf`.

[2] International Energy Agency, "World Energy Outlook 2023," Tech. rep., Paris, 2023. URL `https://www.iea.org/reports/world-energy-outlook-2023`.

[3] Greitzer, E., et al., "N3 Aircraft Concept Designs and Trade Studies," Tech. Rep. NASA CR-2010-216794/VOL1, NASA, 2010.

[4] Liebeck, R. H., "Design of the Blended Wing Body Subsonic Transport," *Journal of Aircraft*, Vol. 41, No. 1, 2004, pp. 10–25. https://doi.org/10.2514/1.9084.

[5] Benad, J., "The flying v a new aircraft configuration for commercial passenger transport," *Proceedings of Deutscher Luft- und Raumfahrtkongress*, Rostock, 2015. https://doi.org/10.25967/370094.

[6] Faggiano, F., and Vos, R., "Aerodynamic design of a Flying V aircraft," *17th AIAA Aviation Technology, Integration, and Operations Conference*, 2017. https://doi.org/10.2514/6.2017-3589.

[7] Van Luijk, N., and Vos, R., "Constrained aerodynamic shape optimisation of the Flying V outer wing," *AIAA AVIATION 2023 Forum*, 2023. https://doi.org/10.2514/6.2023-3250.

[8] Pascual, B. R., and Vos, R., "The effect of engine location on the Aerodynamic efficiency of a Flying-V aircraft," *AIAA Scitech 2020 Forum*, 2020. https://doi.org/10.2514/6.2020-1954.

[9] Empelen, S. v., and Vos, R., "Effect of engine integration on a 4.6%-scale flying-v subsonic transport," *AIAA Scitech 2021 Forum*, 2021. https://doi.org/10.2514/6.2021-0939.

[10] Oosterom, W., and Vos, R., "Conceptual design of a Flying-V aircraft family," *AIAA AVIATION 2022 Forum*, 2022. https://doi.org/10.2514/6.2022-3200.

[11] European Union Aviation Safety Agency, "TYPE-CERTIFICATE DATA SHEET EASA.E.036 for Trent 1000 series engines," Tech. Rep. TE.CERT.00052-002, Rolls-Royce Deutschland Ltd Co KG, April 2024.

[12] European Union Aviation Safety Agency, "TYPE-CERTIFICATE DATA SHEET No. EASA E.111 for Engine Trent XWB series engines," Tech. Rep. TE.CERT.00052-001, Rolls-Royce Deutschland Ltd Co KG, December 2019.

[13] U.S. Department of Transportation, Federal Aviation Administration, "TYPE CERTIFICATE DATA SHEET E00095EN," Tech. Rep. E00095EN, General Electric Company, February 2023.

[14] Clean Sky, Clean Sky 2, Aerospace Technology Institute, Innovate UK, LuFo, Brandenburg State, "UltraFan®: The Ultimate TurboFan," , ????

[15] Roache, P. J., *Verification and Validation in Computational Science and Engineering*, Hermosa Publishers, Albuquerque, NM, 1998.

[16] Menter, F. R., "Two-equation eddy-viscosity turbulence models for engineering applications," *AIAA Journal*, Vol. 32, 1994, pp. 1598–1605. https://doi.org/10.2514/3.12149.

[17] Menter, F. R., "Improved two-equation k-omega turbulence models for aerodynamic flows," Tech. rep., 1992.

[18] Asaro, S., and Vos, R., "Synthesis of the Aerodynamic Model of a Flying Wing Aircraft," *AIAA SciTech*, Orlando, United States of America, January 2025.

[19] Asaro, S., Atmaca, D., van Kampen, E.-J., and Vos, R., "Control Surface Allocation based on Offline Handling Quality Simulations for a Flying Wing Aircraft," *AIAA SciTech*, Orlando, United States of America, 2025.